Identifying Particles in Industrial Systems using MRI Susceptibility Artefacts

Philip Robson and Laurie Hall
Herchel Smith Laboratory for Medicinal Chemistry, University of Cambridge School of Clinical Medicine, Cambridge CB2 2PZ, U.K.

DOI 10.1002/aic.10408
Published online April 7, 2005 in Wiley InterScience (www.interscience.wiley.com).

The potential uses of magnetic susceptibility effects in magnetic resonance imaging (MRI) to identify particles in industrial systems is explored. It is both a practical demonstration, and a review of the literature for experts in both MRI and in industry. The theory of magnetic susceptibility artifacts in MRI is briefly illustrated. Experimental imaging of simplified systems that have relevance to real world processes are explored, and features of those images are related to properties of the system. Data are presented for different sized objects with identical dipole moments, for sub-pixel sized particles for which their potential use as magnetic labels are shown, and, finally, for agglomerations and powders of particles. Given the unique ability of MRI to probe complex, opaque systems, this qualitative interpretation of MRI images, demonstrates that MRI is an important technique for the investigation of material distributions within industrial systems. © 2005 American Institute of Chemical Engineers *AIChE J,* 51: 1633–1640, 2005
Keywords: magnetic susceptibility, magnetic resonance imaging, MRI, particles, precipitates, industrial process systems

Introduction

It is well known that variations in magnetic susceptibility between different regions in a sample can induce distortions in magnetic resonance (MR) images, and fundamental effects have been characterized by considering a simple cylindrical geometry.[1-5] The original motivations for such studies were to understand the artifacts in MR images observed around large air cavities and near to bone-tissue interfaces in the head. Furthermore, it was early recognized that it should be possible to image brain lesions where blood products alter the magnetic susceptibility of nearby tissues.[6,7] More recently the effects of small, sub-pixel sized, super-paramagnetic particles dispersed in water have also been considered[8-12]; here, the magnetic field perturbation around each particle affects the relaxation of the water signal in the bulk of the encompassing pixel. Such systems of particles are being investigated for use as MRI contrast agents in medical imaging. In addition, new imaging sequences have been developed to reduce or compensate for susceptibility effects, particularly for functional MRI echo-planar imaging sequences, which are severely affected by magnetic susceptibility artifacts,[13-16] and for determining fine structures of blood vessels.[17] Furthermore, susceptibility effects are important in NMR spectroscopy studies of heterogeneous samples, including tissues, individual cells, or emulsions or slurries.[18,19]

This article is based on the premise that the majority of industrial and biomedical systems containing one or more particulate components in a fluid matrix will have a characteristic magnetic susceptibility effect to which MRI is sensitive. Examples of such systems previously investigated in this laboratory include: (1) the particles trapped on filter membranes, which usually posses a magnetic susceptibility different from the suspending fluid; also air bubbles trapped on the filter mesh through surface tension effects; and (2) the material precipitated in reactor vessels, which is often magnetically different from the solution.[20,21]

The size and distribution of such particles do not always fall

Correspondence concerning this article should be addressed to L. D. Hall at ldh11@hslmc.cam.ac.uk.

into the two categories outlined above, for which theoretical formulations are possible. Typically, this is when the particles are small in comparison with the image pixel sizes, and form irregular agglomerations, which are on a scale similar to, or larger than the pixel size; thus, the characteristic size of the object is "mesoscopic" in MRI terms, that is, on the scale of a few pixels. The principle of superposition of magnetic fields means that many arrangements of magnetic dipoles could produce the same field at any given point. Therefore, although it is possible to compute the fields around any distribution of magnetic particles, and, hence, simulate the image artifacts produced,[4,22] it is not possible to determine the distribution of magnetic particles from the field pattern measured by imaging techniques.[23] In this article, we consider the potential of magnetic susceptibility effects to provide useful information about the extent and distribution of particles in "real-world" systems and demonstrate the use of those techniques with specific systems.

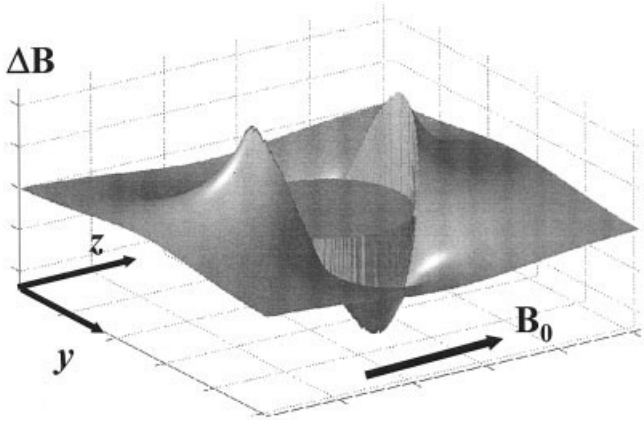

Figure 1. Shift in magnetic flux density strength, ΔB, due to a cylinder, which has a different susceptibility from its surroundings, shown in the plane (*y*-*z*) perpendicular to the axis of the cylinder (along *x*, perpendicular to *y*-*z*) in a main magnetic field along the *z*-axis.

Theoretical Background

Magnetic Resonance Imaging - basics

Only a simple account of magnetic resonance imaging (MRI) is given here; for more detail see any of the excellent texts on magnetic resonance.[24,25,26] MRI is based on the nuclear magnetic resonance (NMR) phenomenon in atomic nuclei. In a strong magnetic field, Zeeman splitting of the hydrogen nuclear spins of water, creates a two-level energy system, transitions between which are stimulated by application of radio-frequency (RF) pulses. As the spin system relaxes toward equilibrium, an RF signal is emitted from the system and received by the scanner. The angular frequency of that signal (the Larmor frequency) is given by $\omega_L = \gamma.B_0$, where γ is the gyromagnetic ratio of the nucleus, and B_0 is the strength of the main magnetic field flux density. This MR signal contains information about the local environment of the spins producing it; for example, the relaxation rates of the water signal from the body differs between various tissues, which gives rise to the image contrast used in medical imaging.

The NMR signal is encoded with spatial information by the application of three linear magnetic field gradients, which are superimposed on the main magnetic field, one in each of the three orthogonal spatial directions. Those gradients make use of the relation between the Larmor frequency and magnetic flux density strength to manipulate the frequency and phase shift of the signal as a function of position; Fourier transformation of that signal results in the MR image.

Magnetic susceptibility

All materials possess some degree of magnetic susceptibility, either diamagnetic or paramagnetic, which is proportional to the applied field strength; it is distinct from ferromagnetism in iron, nickel and cobalt, where magnetic domains are formed that magnify the magnetization of the material many thousands of times. Although magnetic susceptibilities are measured in parts per million, when the material is in the strong magnetic field of the MRI scanner (about 2 T) the resulting effect becomes significant and can be measured.

Susceptibility artifacts in MR images are caused by spatial variations of field strength around any part of an object that has a different magnetic susceptibility to its surroundings, and Schenck has given an excellent description of the basic physics of magnetic susceptibility in MRI.[5] The main magnetic field of the MRI scanner is distorted at the boundaries between regions of different magnetic permeability in the sample; the resulting field patterns can be calculated by solving Laplace's equation, using Maxwell's equations for magnetostatics to determine the appropriate boundary conditions. In general this requires a numerical solution, but for simple geometries, analytical solutions are possible; the dipole field is the simplest solution and is found for cylinders and spheres, and is shown in Figure 1. The dipole field has a universally shaped functional form, and its extent is governed by a parameter termed the magnetic dipole moment *m*, which depends on the main field strength magnetizing the material, the magnetic susceptibilities of the object and its surroundings, and the physical size of the magnetized object.

Since all materials have an intrinsic susceptibility, the appearance of gaseous, liquid, and solid bodies in MR images will be equivalent. For complicated shapes, the resulting field pattern is a summation of dipole, quadrupole, and higher order fields. However, the dipole field pattern decreases slowest with distance and, therefore, it dominates in the "far-field". This will be shown to be a useful property of the induced field when we consider complex assemblages of particles.

Characteristic susceptibility artifact image distortions

Variation in susceptibility within a sample distorts the main magnetic field and results in a spatially varying magnetic field strength. This imparts an additional phase shift to the spins, which distorts the effect of the imaging gradients, and, hence, affects the form of the signal in Fourier-space, resulting in artifacts in the image after Fourier transformation. There are three effects, each of which is demonstrated in the MRI scans, shown in Figure 2, of cylinders with different susceptibilities surrounded by 10 mM aqueous copper sulfate solution (which modifies the relaxation parameters of water in order to reduce the required scanning time); both standard spin echo (SE) and

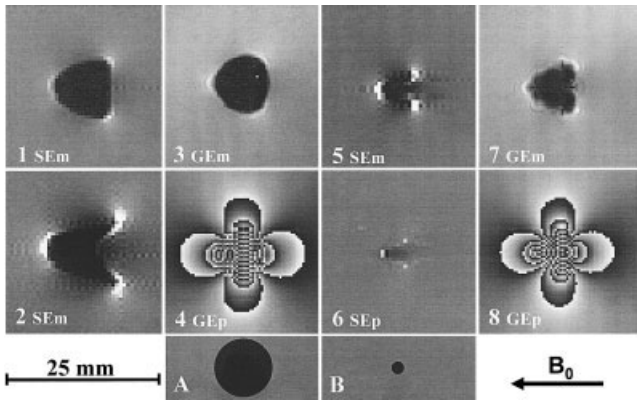

Figure 2. Characteristic image distortions in the plane perpendicular to a cylinder and which includes the main magnetic field vector (right to left in all panels).

The cylinders have different susceptibilities from the surrounding water. Each panel has side 25 mm. Panels 1 and 2 show spin echo magnitude images (denoted SEm). Panels 3, 4, 7, and 8 show gradient echo magnitude (3 and 7) and phase (4 and 8) images (denoted GEm and GEp, respectively) of two different cylinders. Panels 5 and 6 show the magnitude and phase images from a SE sequence (denoted SEm and SEp). Panels A and B show cylinders imaged in panels 1–4 and 5–8, respectively). The radii of the cylinders are 4.0 mm for panels 1 – 4, and 0.95 mm for panels 5 – 8. The susceptibility differences between each cylinder and surrounding water $\Delta\chi$ are 1.81×10^{-5}, and 5.60×10^{-5}, for 1 and 2, respectively, 5.80×10^{-6} for 3 and 4, and 9.41×10^{-5} for 5-8. The resulting magnetic dipole moments m are 2.90×10^{-10}, and 8.97×10^{-10} T.m^2 for 1 and 2, respectively, 9.28×10^{-11} T.m^2 for 3 and 4, and 8.49×10^{-11} T.m^2 for 5–8. For comparison, $\chi_{water} = -9.01 \times 10^{-6}$, $\Delta\chi$ for air is 5.8×10^{-6}, and for a glass tube of radius 4.0 mm, m is 9.28×10^{-11} T.m^2. For both SE and GE sequences, repetition time/echo time TR/TE 500/7.5 ms, slice thickness 10 mm, and a flip angle of 90^0 for GE scans. The resolution in each image is 0.521 mm for 1, 2, 5 and 6, and 0.313 mm for 3, 4, 7 and 8. In the phase images, black corresponds to $+180^0$ and white to -180^0; these show phase wrapping, where a phase of $180^0 + \delta$ is aliased to an angle of $-180^0 + \delta$; zero phase shift is shown grey.

gradient echo (GE) MRI pulse sequences are used[24,25] (and references therein).

Phase shifts

The spatial variation in field strength alters the precessional rate in each small spin-packet such that at the echo the phase accrued by the spin-packet is shifted from that of a reference spin-packet which has experienced no field strength perturbation, by an amount $\Delta\phi = \gamma\,\Delta B\,TE$, where γ is the gyromagnetic ratio for the nucleus, ΔB is the magnetic flux density strength difference from that of the main unperturbed field, and TE is the time to echo. This is only true for gradient echo (GE) sequences. In spin echo (SE) imaging the refocusing pulse reverses the phase accumulation resulting in zero phase shift at the echo time, as shown in Figure 2, panel 6. The phase map pattern around an object is, therefore, a direct representation of the field strength perturbation surrounding it, as is shown in Figure 1 for the simple cylindrical or spherical model. Phase images from a GE sequence for a cylinder are shown in Figure 2, panels 4 and 8; the extent of the phase pattern is similar for these two cylinders of different diameter and susceptibility because the dipole moments are chosen to be approximately equal.

Image distortion

The variation in field strength modifies the linearity of the read-out gradient; hence, the signal emanating from position x in the sample is registered to a point x' in the image such that $g_x\,x' = g_x\,x + \Delta B(x)$, where g_x is the strength of the read-out gradient in the x-direction. For a cylinder, orientated perpendicular to the main field, and for a sphere, the circular cross-section (including the main field B_0) appears as a spear-head shape, as shown in Figure 2, panels 1–3, 5 and 7. The read-out gradient is along B_0. Signal with higher frequency due to the dipole field is transposed to positions further to the left in the image, while the signal with reduced frequency is transposed to the right. $\Delta\chi$ for the cylinder in panel 2 is greater than for panel 1 producing a larger image distortion.

There is no distortion in the phase-encode direction because the encoding depends on the difference in strength between successive applications of the phase-encode gradient, which is insensitive to the static field strength perturbations associated with susceptibility differences. The modification of the field strength across the sample results in nonplanar slices being selected; the RF pulse exciting spins in any location with a Larmor frequency equal to the RF frequency. Distortion is the same for both SE and GE images, and is greater for weaker read-out gradients g_x, and for greater field strength perturbations, ΔB.

Signal magnitude effects

The miss-registration of signal in the images results in a focusing of the signal intensity in the image, which produces bright and dark regions in the image, as seen in Figure 2, panels 1–3, 5 and 7. These are more pronounced in SE images where no phase shifts occurs (Figure 2, panels 1, 2 and 5); whereas, in GE images the phase shifts tend to result in destructive addition of the signal such that the bright spots are less pronounced (Figure 2, panels 3 and 7).

Importantly, the dephasing of the signal in GE images produces a signal void in the image that is larger than the physical volume of the particle; this apparent volume of the particle is a useful property, which will be discussed below. Furthermore, the dephasing in GE images produces finer and more complicated structure in the magnitude image when the field gradients surrounding the particle are relatively large, that is, the particle susceptibility is high; this is shown in Figure 2, panels 3 and 7 where the cylinder susceptibility is higher in panel 7. Panels 5–8 show images of the same sample cylinder, and, therefore, highlight the different appearance of magnetic susceptibility effects seen in GE as opposed to SE images.

Experimental

All MRI scanning was carried out using a 2 T, 31 cm bore, Oxford Instruments superconducting magnet interfaced with an Oxford Research Systems console utilizing a BRUKER ASPECT 3000 running TOMIKON 890601.0 software (Bruker Medizin Technik GmbH, Karlsruhe, Germany). The gradient coils (20-cm dia., 13 mT/m max strength) and transverse resonator RF coil (6.5-cm dia.) were built in HSLMC. Scan details

for all images are included in the text and figure captions. The raw data were converted to MR images using CaMReS software written by Dr. N. J. Herrod in HSLMC.

MRI measurement of dipole moment

As described previously, the field perturbation due to an object depends on its shape, the difference between the material's susceptibility and that of the surrounding fluid, and the strength of the main magnetic field. The precise structure of the material is unimportant, the magnetic susceptibility being a bulk macroscopic property. Distinguishing objects of different materials, which are of the same shape, is achieved by determining their dipole moments. We employ a method to measure the dipole moment based on the phase image[27,28]; other authors have used a method based on the magnitude images.[29] As shown in the theoretical background section the phase image around an object produced by a GE sequence is equivalent to a map of the field induced by the object. The dipole moment is measured by relating the strength of that field to its extent. Equation 1 gives the phase shift $\Delta\phi$ due to a field strength perturbation ΔB

$$\Delta\phi = \gamma \cdot \Delta B \cdot TE \tag{1}$$

where γ is the gyromagnetic ratio and *TE* is the time to echo. ΔB is the product of the magnetic dipole moment *m,* and a geometrical function *f(θ, r),* where θ is the polar angle and *r* is the radius, with *m*, for a cylinder of radius *a*, with a susceptibility different from its surroundings by an amount $\Delta\chi$, given by Eq. 2

$$m = \frac{a^2 \cdot \Delta\chi \cdot B_0}{2} \tag{2}$$

Measuring the width $2r_\pi$, between points where $\Delta\phi = \pi$ on the phase image, where $\theta = \pi/2$, the dipole moment *m* can be determined in terms of *TE* and r_π (Eq. 3).

$$m = \frac{\pi \cdot r_\pi^2}{\gamma \cdot TE} \tag{3}$$

Choosing $\theta = \pi/2$ to correspond to the phase-encode direction is done because there is no image distortion in this direction and hence the width of the phase map in this direction is not affected. Furthermore, the distortion seen in the frequency-encode direction at this radius (that is, this field strength perturbation) is always small, and dephasing is minimal.

The dipole moments of various cylindrical samples with different diameters and material susceptibilities were measured from the phase map of a standard gradient echo sequence (TR/TE 500/7.5 ms, flip angle 90^0), and the values compared to those calculated from Eq. 2. Small glass or plastic tubes, filled with either air or a manganese chloride solution, were placed coaxially in a cylindrical glass jar 5 cm in dia. and 5 cm tall filled with 10 mM aqueous copper sulfate solution. Variation of the concentration of the manganese chloride solution changes the magnetic susceptibility of the cylinder. An effective susceptibility must be calculated to include the effect of the glass

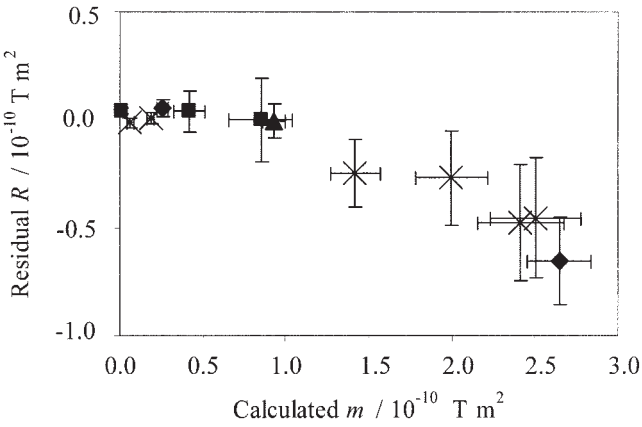

Figure 3. Accuracy of measurement of dipole strength *m* from the phase map of a standard GE sequence (TR/TE 500/7.5 ms, flip angle 90^0), as compared to the value calculated from the physical parameters of the sample, cylinder diameter, material susceptibility, and solution concentration.

The residual R is the difference between MRI measurement and calculated value, and is plotted against the calculated value of *m*. Marker style represents outer radius of the cylinder: squares 0.95 mm, crosses 1.6 mm, diamonds 2.45 mm, triangles 4.0 mm.

or plastic tube[30]. The phase map of a reference scan with no cylinder present was subtracted from the experimental scan in order to remove the phase variation due to inhomogeneities of the main field. The data in Figure 3 demonstrate that MRI provides a good measurement of dipole moment for the cylindrical system for dipole moments up to $\sim 2 \times 10^{-10}$ T.m^2, above which the measurement becomes progressively smaller than the true value. Our experiments also show that MRI measures the dipole to be increasingly weaker at progressively larger echo times. There are some variations of the measured dipole strength when the same cylinder is measured at different strengths of the frequency gradient; however, these are within the estimated error and, therefore, considered to be negligible. No trend between cylinder radius and accuracy of dipole strength measurement was found.

Thus, although it is possible to measure the dipole moment of an object using MRI, such measurements do not give a reliable value; hence, the comparison between the measured dipole moments of two different objects is the most reliable way to distinguish two objects from one another through their susceptibilities. For a particle to be measured in this way requires that a phase shift of about π be induced in the image, and that the associated phase pattern in the image be resolvable. This depends on the protocol echo time and the magnetic moment of the sample, the latter being a function of particle size, susceptibility and the main field strength; it must also be considered whether enough magnetic resonance signal remains at the echo time required. Thus, it is possible that a particle with a very high susceptibility will not be observable if it is too small, whereas the field around a large object with a very low susceptibility will be observable, which may seem counter-intuitive.

Table 1 gives the values of susceptibility with respect to

Table 1. Susceptibility Differences with Respect to Water for Materials Relevant to some Industrial Applications and some Materials (*) Commonly Used for NMR Sample Tubes[†]

Material	Susceptibility Difference/ppm	Cylinder Diameter/mm	Dipole Moment Strength/T m^2
Air	+9.4	10	$+2.34\ 10^{-10}$
Glass* (pure SiO_2)	−4.6	10	$-1.15\ 10^{-10}$
Oxygen	+10.8	10	$+2.69\ 10^{-10}$
Copper	−0.68	10	$-1.7\ 10^{-11}$
Carbon (graphite)	−4.8	10	$-1.2\ 10^{-10}$
Air	+9.4	0.1	$+2.3\ 10^{-14}$
Glass* (pure SiO_2)	−4.6	0.1	$-1.15\ 10^{-14}$
Pyrex* (Borosilicate)	−1.8	0.1	$-4.5\ 10^{-15}$
Zirconia* (ZrO_2)	+0.21	0.1	$+5.25\ 10^{-16}$
Ultrem* (*p*-etherimide)	+0.088	0.1	$+2.2\ 10^{-16}$
Iron oxide (Fe_2O_3)	+1490	0.1	$+3.73\ 10^{-12}$
Iron oxide (FeO)	+7570	0.1	$+1.89\ 10^{-11}$
Gadolinium oxide (Gd_2O_3)	+13048	0.1	$+3.26\ 10^{-11}$
Uranium oxide (UO_2)	+1214	0.1	$+3.03\ 10^{-12}$
Aluminium oxide (Al_2O_3)	−9.1	0.1	$-2.27\ 10^{-14}$
Lanthanum sulphate	−3.8	0.1	$-9.5\ 10^{-15}$
Carbon (graphite)	−4.8	0.1	$-1.2\ 10^{-14}$

[†]Values are appropriate for magnetic fields given in SI units. Also shown are the magnetic dipole moments for a cylinder of each material, with the given diameter, in a main field of 2 T. Values for susceptibility are taken from[31], except for (*) from[32].

water of materials that are of relevance to some industrial applications and some materials commonly used for NMR sample tubes; also shown are the resulting magnetic dipole moments for various sizes of a cylinder of the material in a main field of 2 T. Dipole moment m is given by Eq. 2.

Sub-pixel sized particles

The field induced by a particle of high susceptibility has a wide extent and, thus, produces a wide artifact in an MR image. The large field gradients near the particle produce a loss of signal in GE images resulting in a signal void several times larger than the volume of the particle. For large objects, the overall effect can destroy much of the image; however, for small, sub-pixel sized particles, this effect makes them observable in an image[12]. This *spatial amplification* effect of magnetic particles, which would otherwise be too small to be detected by MRI, can be used for labeling in particulate systems to probe spatial and temporal effects, for example, particle deposition on a filter bed, or particle migration in a porous medium; and to label reactant molecules. Figure 4 shows the appearance of a small volume of gadolinium oxide powder (Gd_2O_3), formed into a ball shape about 1 mm diam., and held on the end of a copper wire with wax tape; for Gd_2O_3 and water, $\Delta\chi = 13048$ ppm.

Panels 1 and 2 are the magnitude and phase images of a GE sequence, while 3 and 4 are corresponding images from a SE sequence; together, they demonstrate the differences between the effects seen in GE and SE imaging. The signal void in panel 1 is between 6 and 7 times wider than the size of the powder spot. The SE image in panel 3 shows reduced signal loss with an associated high contrast pattern of bright and dark spots. The GE phase map shown in panel 2 corresponds to the dipole field induced by the powder spot. There is a nonzero phase map seen in SE imaging, however, it is less extensive than, and not as well formed as in GE imaging.

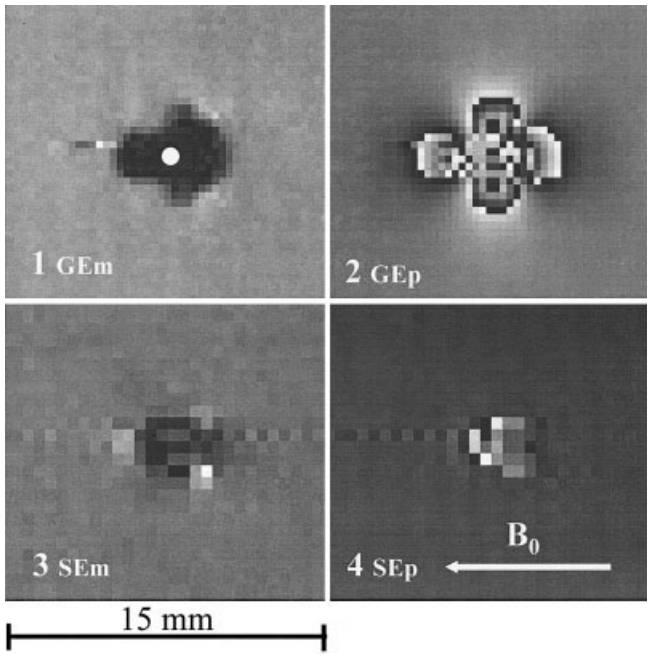

Figure 4. 2-D SE and GE images (magnitude and phase images denoted SEm, SEp, GEm, and GEp) show the spatial amplification effect of the high susceptibility difference between gadolinium oxide powder (Gd_2O_3) and water ($\Delta\chi$ = 13048 ppm).

The powder is formed into a ball shape about 1 mm diam., and held on the end of a copper wire with wax tape (for copper and wax $\Delta\chi$ with respect to water is approximately zero). All panels are of side 15 mm, the main field is in the plane and right to left, with the powder spot in the imaging plane. The white spot in the center of panel 1 is the gadolinium oxide powder spot. For panels 1 and 2, a standard GE sequence was used with TR/TE 500/7.5 ms and a flip angle of 90^0, FOV/matrix/resolution is 8x8 cm, 256 × 256, 313 μm, with slice thickness 1 mm; for panels 3 and 4, a standard SE sequence was used with TR/TE 500/6 ms, FOV/matrix/resolution is 6.67 × 6.67 cm, 128 × 128, 523 μm, with slice thickness 2 mm.

Identification of irregular dispersions of particles

A definitive distinction between two particles of different materials can be made when one material is more, and the other less, magnetically susceptible than the surrounding water. The phase images around such particles show opposite polarity; also the image distortion is in the opposite direction. This is the case for air and glass, as shown in Figure 5; in panels 1 and 2 a ping-pong ball is placed next to a glass bead (dia. 20 mm and 9 mm, respectively), and both are suspended in gel made from cooking gelatine.

For large particles where the phase pattern around the particle is resolvable, the method for measuring dipole moment

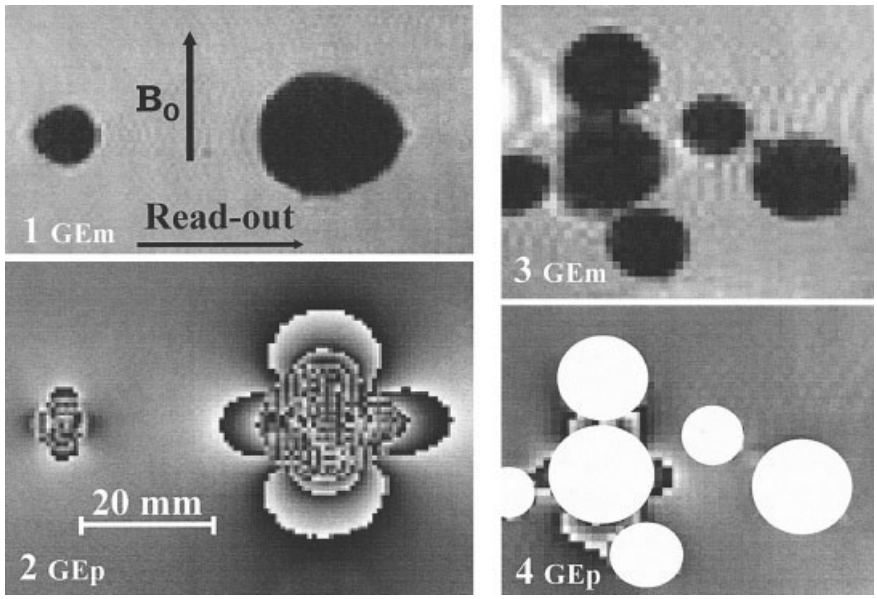

Figure 5. Panels 1 and 2 show GE magnitude and phase images (GEm and GEp) of a glass bead, respectively, (left) and an air-filled plastic ball (right), (dia. 20 mm and 9 mm, respectively), and demonstrate the distinction between the two materials via characteristic magnetic susceptibility effects.

Panels 3 and 4 show GE magnitude and phase images respectively of a collection of plastic beads (all about 15 mm dia.) and one glass bead, and demonstrate the localization of the glass bead by identifying its characteristic phase pattern. Particles are suspended in cooking gelatine (4 wt %), dissolved in aqueous copper sulfate (10 mM), which remains set at room temperature, inside a 6 cm dia. plastic bottle, and imaged using a standard 3-D GE sequence with TR/TE 100/7.5 ms and flip angle of 90^0, with FOV $16 \times 8 \times 8$ cm (long direction along read-out, left to right), with matrix 256 x 128 x 128 giving isotropic resolution of 0.625 mm for panels 1 and 2, and with matrix $128 \times 64 \times 64$ giving an isotropic resolution of 1.25 mm for panels 3 and 4. The main field is in the plane and shown by the arrow in panel 1 for all images.

described in the section on MRI measurement of dipole moment can be used, and the size of the particle can be measured from a SE image; hence, susceptibility can be determined from these two measurements and the material of the particle identified.

Figure 5, panels 3 and 4, show the power of phase imaging to identify a particle of a species with high susceptibility among others with low susceptibility; this is important to particle labeling applications discussed earlier in the section on sub-pixel sized particles. One glass bead is suspended adjacent to several plastic ones in gel (all ~15 mm dia.); the susceptibility difference between plastic and gel is much less than that between glass and gel, therefore, the phase image shows the characteristic pattern around the glass bead, but no significant induced dipole field around the plastic beads.

Where the particles are smaller than the pixels (as is the likely case for powders and precipitates), it is not possible to identify the individual field around each one; furthermore, since the fields around the particles superimpose upon one another, measurement of dipole moments is impossible, precluding material identification. However, progress can be made by combined use of: (1) SE magnitude imaging, which reflects the physical volume occupied by the material; (2) GE magnitude imaging, where the extent of signal loss in the GE image reflects the degree of *spatial amplification* due to the high susceptibility material present; and (3) GE phase images, which represent the fields induced on the material; together, with some knowledge of the susceptibility of the particles involved, we can tell if a dark region in an image is due to a large continuous material or a more disperse distribution of powder which has a relatively high susceptibility and gain some knowledge of the distribution of a material.

We demonstrate this by examples shown in Figure 6. In Figure 6a a powder of high susceptibility (iron oxide) is deposited on a sponge cube, of side about 1 cm, and imaged using standard 2-D SE and GE sequences. The spatial amplification effect results in a large region of signal void around the area occupied by the powder in the GE image (panel 2), as if it was a single large object, for example, an air cavity. However, the SE image (panel 1) is not dephased by the field perturbation and does not suffer signal loss; rather it appears as a speckle pattern due to the focusing of signal intensity associated with the image distortion. Therefore, since a SE image of a single continuous air cavity would also show a dark void (similar to the GE image in panel 2), we can infer that these images are of a disperse powder.

Distinguishing one dispersed material from another, or the relative abundance of two materials present in a region, is more difficult but possible. If the material has low susceptibility (as for aluminum oxide), then the difference between SE and GE magnitude images will be small, the signal void being due to displaced water; if the powder has high susceptibility (as for iron oxide), the difference is quite marked (as seen in Figure 6a) due to the spatial amplification effect with the additional amount of signal lost being related to the volume of the high susceptibility material.[12]

GE phase images provide much insight into the make-up and distribution of a dispersed system of particles. To demonstrate this, we imaged air bubbles trapped in a sponge cube and compared them to those of iron oxide trapped on the sponge

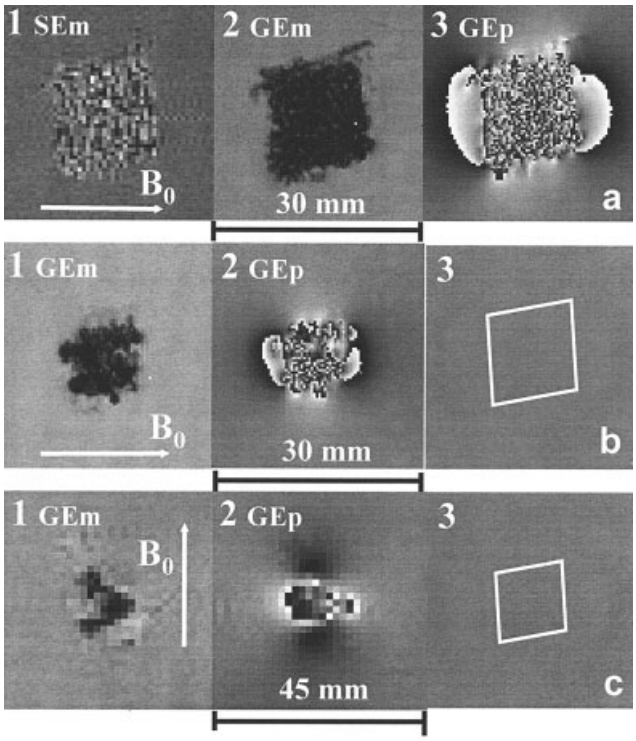

Figure 6. (a) SE and GE magnitude (SEm and GEm), and GE phase (GEp) images, respectively, showing iron oxide (Fe_2O_3) powder (< 5 μm) trapped on a sponge (SE and GE sequences have TR/TE 500/6 ms and 500/7.5 ms respectively, and flip angle 90^o for GE; the FOV/matrix/resolution was 6.67 × 6.67 cm/128x128/521 μm and 8 × 8 cm/256x256/313 μm for SE and GE, slice thickness was 2 mm.); (b) and (c) 2-D GE magnitude and phase images showing air bubbles trapped in a sponge, with TR/TE 500/7.5 ms and flip angle 90^o, FOV/matrix/resolution is 8x8 cm/256x256/313 μm, and slice thickness is 2mm for Figure 6b; those in Figure 6c were acquired using a 3D GE sequence with TR/TE 100/7.5 ms and flip angle of 90^o, FOV/matrix resolution is 16 × 8 × 8 cm/128 × 64 × 64/1.25 mm.

Panel 3 in both Figure 6b and 6c show the sponge cube in Figure 6a, b, and c, respectively.

shown in Figure 6a. The images in Figure 6b were acquired with a standard 2-D GE sequence and those in Figure 6c with a standard 3-D GE sequence. The curved shapes in the phase image of Figure 6b indicate that the field perturbation around the sponge is a sum of a few localized fields; these are the well-defined dipole fields on individual bubbles trapped on the sponge. This is in contrast to the phase pattern in Figure 6a where the field due to iron oxide powder is smoother and follows the square shape of the sponge, showing that the iron oxide powder is evenly distributed on the sponge. The phase image in Figure 6c demonstrates the usefulness of the far-field limit of the induced magnetic field. The shape of the perturbing object (the air bubbles) is noncircular in this slice, therefore, the induced field has dipole, quadrupole and higher-order components; yet in the far-field the phase image shows a dipole field, from whose polarity we can ascertain that the object has, in this case, a magnetic susceptibility greater than water.

Conclusions

We have given a broad demonstration of the ways in which the appearance of susceptibility artifacts in MR imaging can be used to identify different materials. Although we have not focused on schemes to quantify either material volume or material susceptibility, we have included references to authors who have undertaken such studies. While the latter is possible, we have shown that one method of measuring the dipole moment of a cylinder is not accurate for all such values and, therefore, is not a definitive method for particle identification that should be used on its own. Although other methods of measuring susceptibilities exist, we feel that there is great benefit from MR imaging alone; we have shown that the combined use of SE and GE magnitude imaging and GE phase imaging provides insight into differentiation of two materials, and into the relative distribution of two dispersed materials. However, there is no definitive procedure to be employed to every system; rather, the principles developed here must be tailored to each system of interest. This involves adjusting MRI scan parameters, such as echo times or gradient strengths or investigating a model system where the magnetic properties of the materials are modified, either by labeling with more magnetic material, or substitution with less magnetic material, to suit the MRI techniques.

Despite these potential drawbacks, MRI offers a unique opportunity to investigate the spatial and temporal evolution of real industrial systems; the method is noninvasive and three-dimensional (3-D), and so the system of interest can be probed without perturbing the flow, deposition or functioning of the system. Furthermore, providing the system is transparent to radio-frequency radiation, the MRI method enables 3-D investigation of optically opaque process fluids and complex systems, such as porous media, where the material of interest is occluded by the vessel itself; clearly this is important for many real industrial systems.

Acknowledgments

It is a pleasure to acknowledge that this work was supported by an Endowment from the late Dr Herchel Smith.

Literature Cited

1. Ludeke KM, Roschmann P, Tischler R. Susceptibility artefacts in NMR imaging. *Magn Reson Imag*. 1985;3:329-343.
2. Posse S, Aue WP. Susceptibility artifacts in spin echo and gradient echo imaging. *J Magn Reson*. 1990;88:473-492.
3. Yamanda N, Imakita S, Sakuma T, Nishimura Y, Yamanda Y, Naito H, Nishimura T, Takamiya M. Evaluation of the susceptibility effect on the phase images of a simple gradient echo. *Radiology*. 1990;175: 561-565.
4. Bakker CJG, Bhagwandien R, Moreland MA, Fuderer M. Susceptibility artifacts in 2DFT spin echo and gradient echo imaging: the cylinder model revisited. *Magn Reson Imag*. 1993;11:539-548.
5. Schenck JF. The Role of Magnetic Susceptibility in magnetic resonance imaging: MRI magnetic compatibility of the first and second kinds. *Med Phys*. 1996;23(6):815-850.
6. Young IR, Khenia S, Thomas DGT, Davis CH, Gadian DG, Cox IJ, Ross BD, Bydder GM. Clinical magnetic susceptibility mapping of the brain. *J Comput Assist Tomogr*. 1987;11(1):2-6.

7. Schenck JF. Magnetic resonance imaging of brain Iron. *J of the Neurological Sciences*. 2003;207:99-102.
8. Weisskoff RM, Zuo CS, Boxerman JL, Rosen BR. Microscopic susceptibility variation and transverse relaxation: theory and experiment. *Magn Reson Med*. 1994;31:601-610.
9. Yablonskiy DA, Haacke EM. Theory of NMR signal behaviour in magnetically inhomogeneous tissues: the static dephasing regime. *Magn Reson Med*. 1994;32:749-763.
10. Yablonskiy DA. Quantitation of intrinsic magnetic susceptibility related effects in a tissue matrix phantom study. *Magn Reson Med.* 1998;39:417-428.
11. Bowen CV, Zhang X, Saab G, Gareau PJ. Application of the static dephasing regime theory to superparamagnetic iron-oxide loaded cells. *Magn Reson Med*. 2002;48:52-61.
12. Bos C, Viergever MA, Bakker CJG. On the Artifact of a subvoxel susceptibility deviation in spoiled gradient-echo imaging. *Magn Reson Med*. 2003;50:400-404.
13. Jezzard P, Balaban RS. Correction for geometric distortion in echo planar images from B_0 field variations. *Magn Reson Med*. 1995;34: 65-73.
14. Cordes D, Turski PA, Sorenson JA. Compensation of susceptibility-induced signal loss in echo-planar imaging for functional applications. *Magn Reson Imag*, 2000;18:1055-1068.
15. Song AW. Single shot EPI with signal recovery from the susceptibility-induced losses. *Magn Reson Med*. 2001;46:407-411.
16. Weiger M, Pruessmann KP, Osterbauer R, Bornert P, Boesiger P, Jezzard P. Sensitivity-encoded single-shot spiral imaging for reduced susceptibility artifacts in BOLD fMRI. *Magn Reson Med*. 2002;48: 860-866.
17. Robinson SP, Rijken PFJW, Howe FA, McSheehy PMJ, van der Sanden BPJ, Heerschap A, Stubbs M, van der Kogel AJ, Griffiths JR. Tumor vascular architecture and function evaluated by non-invasive susceptibility MRI methods and immunohistochemistry. *J Magn Reson Imag*. 2003;17:445-454.
18. Chu SC-K, Xu Y, Balschi JA, Springer Jr CS. Bulk magnetic susceptibility shifts in NMR studies of compartmentalized samples: use of paramagnetic reagents. *Magn Reson Med.* 1990;13:239-262.
19. Kuchel PW, Chapman BE, Bubb WA, Hansen PE, Durrant CJ, Hertzberg MP. Magnetic susceptibility: solutions, emulsions and cells. *Concepts Magn Reson*. 2003;18A(1):56-95.
20. Dirckx CJ, Clark SA, Antalek B, Tooma J, Hewitt JM, Kawaoka K, Hall LD. Magnetic Resonance Imaging of the Filtration Process. AIChE J. 2000;46(1):6-14.
21. Nott KP, Paterson-Beedle M, Macaskie LE, Hall LD. Visualisation of metal deposition in biofilm reactors by three-dimensional magnetic resonance Imaging. *Biotech Letts*. 2001;23:1749.
22. Truong T-K, Clymer BD, Chakeres DW, Schmalbrock P. Three dimensional numerical simulations of susceptibility-induced magnetic field inhomogeneities in the human head. *Magn Reson Imag*. 2002;20: 759-770.
23. Li S, Dardzinski BJ, Collins CM, Yang QX, Smith MB. Three dimensional mapping of the static magnetic field inside the human head. *Magn Reson Med*. 1996;36:705-714.
24. Chen C-N, Hoult DI. *Biomedical Magnetic Resonance Technology*. Bristol: IOP Publishing, Ltd., 1989.
25. Wehrli FW, Shaw D, Kneeland JB. *Biomedical Magnetic Resonance Imaging: Principles, Methodology, and Applications*. New York: VCH Publishers Inc., 1988.
26. Callaghan PT. *Principles of Nuclear Magnetic Resonance Microscopy*. Oxford: Clarendon Press, 1991.
27. Wang ZJ, Li S, Haselgrove JC. Magnetic resonance imaging measurement of volume magnetic susceptibility using a boundary condition. *J Magn Reson*. 1999;140:477-481.
28. Li L. Magnetic susceptibility quantification for arbitrarily shaped objects in inhomogeneous fields. *Magn Reson Med*. 2001;46:907-916.
29. Beuf O, Briguet A, Lissac M, Davis R. Magnetic resonance imaging for the determination of magnetic susceptibility of materials. *J Magn Reson*. 1996;112:111-118.
30. Lucas AJ, Gibbs SJ, Jones EWG, Peyron M, Derbyshire JA, Hall LD. Diffusion Imaging in the presence of static magnetic field gradients. *J Magn Reson*. 1993;104:273-282.
31. Lide DR. *CRC Handbook of Chemistry and Physics*, 83rd Ed. Boca Raton: CRC Press LLD, 2002.
32. Doty Scientific sales literature, 2004.

Manuscript received Feb. 3, 2004 and revision received Sept. 10, 2004.